THE JOURNAL OF PHYSICAL CHEMISTRY C

Article

pubs.acs.org/JPCC

CO Dissociation on Face-Centered Cubic and Hexagonal Close-Packed Nickel Catalysts: A First-Principles Study

Jin-Xun Liu,[†,‡] Bing-Yan Zhang,[‡] Pei-Pei Chen,[‡] Hai-Yan Su,[‡] and Wei-Xue Li*[,†,‡]

[†]College of Chemistry and Material Sciences, iChEM (Collaborative Innovation Center of Chemistry for Energy Materials), CAS Center for Excellence in Nanoscience, Hefei National Laboratory for Physical Sciences at the Micro-scale, University of Science and Technology of China, Hefei, China

[‡]State Key Laboratory of Catalysis, State Key Laboratory of Molecular Reaction Dynamics, Dalian Institute of Chemical Physics, Chinese Academy of Sciences, Dalian 116023, China

Supporting Information

ABSTRACT: Exploring the dependence of the structure−activity relationship of catalysts is important for improving the activity and selectivity in heterogeneous catalysis. Among other factors, the influence of the crystal phases, face-centered cubic (FCC) and hexagonal close-packed (HCP), of Ni catalysts on CO dissociation is studied by density functional theory (DFT). Surface energies of numerous FCC and HCP facets are calculated to construct the corresponding morphologies, and the exposed facets (six facets for FCC Ni and five facets for HCP Ni) are used to investigate the CO dissociation. For FCC Ni, (311) is the most active facet with the least barrier of 1.58 eV, followed by (100) and (211) with barriers of 1.63 and 1.75 eV, respectively. For HCP Ni, $(10\bar{1}2)$ is the most active facet with the least barrier of 1.73 eV, followed by $(10\bar{1}1)$ with a barrier of 1.86 eV. On both FCC and HCP Ni, CO dissociation shows a dramatic structural sensitivity irrespective of direct or H-assisted pathway. Compared to the direct dissociation, the H-assisted dissociation is kinetically favorable on both FCC and HCP Ni. With increase of dissociation barrier, the preferred dissociation pathway changes from COH intermediate to CHO intermediate. FCC Ni can expose abundant facets with low barrier. The result is compared with more active cobalt catalysts showing an opposite dependence on the crystal phases. The revealed insights regarding the crystal phase and the composition of catalysts upon activation of the diatomic molecules provide a new perspective for rational design of catalysts to expose more active sites for a higher specific activity.

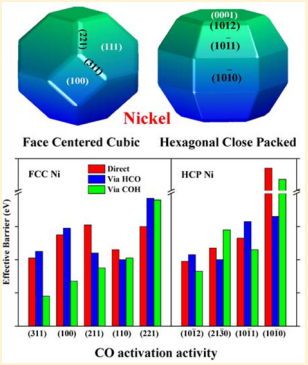

1. INTRODUCTION

Understanding the structure−activity relationship of reactions is of great significance for rational design of catalysts in heterogeneous catalysis. The particle size,[1−8] support,[9,10] and morphology[11−14] and the formation of interface[15−19] and alloy[20] have been shown to have a dramatic influence on the activity and selectivity of catalysts.[21] Recently, the influence of the crystal phase of catalysts on structure−activity relationship has attracted increasing interest.[8,22−37] Co catalysts with a hexagonal close-packed (HCP) phase were found to have a higher Fischer−Tropsch synthesis (FTS) activity compared with the catalysts with a face-centered cubic (FCC) phase.[22−25,38] So far, pure HCP phase Co and FCC phase Co catalysts remain difficult to synthesis because the phase transition between HCP and FCC phase depends sensitively on particle size, reaction temperatures and pressures, support, and sample pretreatment.[39−42] On the basis of density functional theory (DFT) calculations, we found that the HCP Co has a higher activity of CO dissociation due to the presence of the denser and favorable sites, which were not available on FCC Co otherwise.[43] Ru catalysts showed phase- and size-dependent activity for CO oxidation: when the particle size was larger than 3 nm, the FCC Ru particles were more reactive than the conventional HCP Ru particles. With decrease of particle size, HCP Ru particles became more active.[28,36] A recent work showed that the enhancement of the CO oxidation activity in FCC Ru catalyst may be caused by an increase in imperfections due to lattice distortions of close-packed planes and static atomic displacements.[35] Ni is an efficient catalyst for CO methanation.[44−46] Bulk Ni adopts a FCC phase under ambient conditions but could transform to a HCP phase when the particle size was less than 4 nm.[47] Moreover, HCP Ni particles could be synthesized via chemical methods[48−55] and even via a one-pot chemical route.[56] However, it remains open to explore the influence of Ni crystal phases on CO methanation.

CO dissociation on transition-metal surfaces has been studied extensively. It is structural highly sensitive and can dissociate via a so-called direct pathway CO → C + O or indirect pathway assisted by hydrogen via CO + H → HCO → CH + O and CO + H → COH → C + OH.[14,43,57−64] The structure sensitivity of CO activation was also found on Ni, and the under-coordinated sites were concluded to be active sites.[65,66] Moreover, the H-assisted CO activation via a COH intermediate was suggested to be the rate-determining step for

Received: August 30, 2016
Revised: October 9, 2016
Published: October 12, 2016

DOI: 10.1021/acs.jpcc.6b08742
J. Phys. Chem. C 2016, 120, 24895−24903

methanation on Ni catalysts.[46,67] Our calculations on cobalt showed that CO dissociation depends sensitively on the crystal phases: direct pathway on HCP Co but H-assisted pathway on FCC Co.[43] Despite numerous studies to date, the influence of Ni crystal phases on CO dissociation, the crucial step for CO methanation, remains unclear. Moreover, it is also unclear how the presence of hydrogen changes the CO dissociation pathway as well as its dependence on crystal phases. Because Ni and Co catalysts have clearly distinct selectivity in syngas conversion, investigations of Ni crystal phases influence on CO dissociation and its comparison with Co would be valuable for the optimization of selectivity.

We present here a systematic DFT study of CO dissociation on FCC and HCP Ni. Wulff construction based on calculated clean surface energies of numerous FCC and HCP Ni facets is used to derive the corresponding morphologies. From the morphologies optimized, the exposed facets are used as a playground to explore the influence of crystal phases. On each of the exposed facets, three reaction pathways, namely, direct dissociation and H-assisted CO dissociation via HCO and COH intermediates, are calculated. The structure sensitivity of CO activation on Ni crystal phases is discussed. Finally, the present result is compared with our previous work on cobalt.

2. COMPUTATIONAL DETAILS

All the spin-polarized DFT calculations were performed using the Vienna ab initio simulation package (VASP).[68,69] We have used projector augmented wave (PAW)[70] potentials and the Perdew−Burke−Ernzerhof (PBE) functionals[71] throughout this paper without mention otherwise. The plane wave cutoff energy was specified by 400 eV, and the convergence threshold for geometry optimizations was set to 1×10^{-4} eV. The geometry optimizations were considered to be converged when all the forces on atoms were less than 0.02 eV/Å. We have used Monkhorst−Pack k-points sampling[72] of $8 \times 8 \times 8$ and $12 \times 12 \times 8$ for the lattice parameters calculations for FCC and HCP Ni, respectively. The determined equilibrium lattice constants for bulk FCC and HCP Ni are $a = b = c = 3.525$ Å and $a = b = 2.489$, $c = 4.091$ Å, which are consistent with experimental values of 3.524 Å for FCC Ni[73] and $a = b = 2.50$, $c = 3.98$ Å for HCP Ni,[74] respectively. To obtain accurate surface energies, we have adopted p(1×1) slab models with the atomic layers of at least 20 Å separated by a vacuum of 15 Å for the low-index FCC and HCP Ni surfaces. All the atoms in the slab are fully relaxed. Monkhorst−Pack k-points sampling of $12 \times 12 \times 1$ was used for the FCC Ni (111) surface, scaled for the other surface energies calculations.

The p(2×2) slab models were used for the calculation of CO activation on all the facets exposed on the morphologies of FCC and HCP Ni. All the surfaces were simulated by using four equivalent (111) atomic layers (except for FCC Ni (100) surface with five layers) slabs. Neighboring slabs were separated by a vacuum of 15 Å to avoid the interactions between them. The density of k-points was kept at ~0.04 $Å^{-1}$. All the adsorbates and the topmost two equivalent (111) atom layers were relaxed. We have used the improved force reversed method[75] to locate the transition states (TS), and the force tolerance of 0.03 eV/Å was adopted without zero-point energy correction. Some of the TSs are verified by climbing-image nudged elastic band (CI-NEB) methods.[76,77] We carried out frequency analysis to confirm the TS with only one imaginary frequency.

The surface energy is determined by $E_{sur} = (E_{slab} - NE_{bulk})/2A$, where E_{slab} and E_{bulk} are the total energies of the slab and one bulk Ni atom, respectively. N is the number of Ni atoms in the slab, and A is the surface area. The adsorption or binding energy (E_{ads}) of the intermediate A can be calculated as $E_{ads} = E_{A/slab} - E_{slab} - E_A$, where $E_{A/slab}$ and E_{slab} are the total energies of the slab with chemisorbed species A and the clean surface, respectively, and E_A is the energy of radical or molecule A in the gas phase. A negative E_{ads} means an exothermic adsorption or binding. The elementary reaction energies ΔE are calculated as the difference between the total energies of the products and the reactants. We chose the separate most stable adsorbed fragments on the surface as the initial and final states.

3. RESULTS

3.1. Morphology of FCC and HCP Ni. Bulk FCC and HCP Ni have different symmetries, O_h and D_{3h} point group, respectively. Though both are close-packed with 12-coordination number for bulk atom in the first nearest neighbor, the different symmetries result in distinct morphology. This could be decisive in the reactivity of FCC and HCP Ni, as indeed shown below. To see this clearly, we first calculated the surface energies of all the low Miller-index facets of FCC and HCP Ni and derived the corresponding morphologies based on the principles of Wulff construction. The calculated surface energies and the derived morphologies of FCC and HCP Ni are shown in Table 1 and Figure 1, respectively.

Table 1. Calculated Surface Energies (E_{sur}, in meV/Å^2) for the Low-Index Facets of FCC and HCP Ni[a]

FCC Ni					
(*hkl*)	E_{sur}	S_p	(*hkl*)	E_{sur}	S_p
(111)	121	60	(311)	143	7
(221)	136	8	(321)	145	0
(100)	138	18	(320)	149	0
(211)	139	4	(310)	149	0
(110)	143	2	(210)	150	0
HCP Ni					
(*hkil*)	E_{sur}	S_p	(*hkil*)	E_{sur}	S_p
(0001)	115	18	(11$\bar{2}$0)	139	0
(10$\bar{1}$0)A	122	26	(11$\bar{2}$1)	144	0
(10$\bar{1}$1)A	126	48	(20$\bar{2}$1)B	147	0
(20$\bar{2}$1)A	129	0	(21$\bar{3}$0)B	149	0
(21$\bar{3}$0)A	136	2	(10$\bar{1}$1)B	156	0
(10$\bar{1}$2)A[b]	137	6	(10$\bar{1}$0)B	160	0
(10$\bar{1}$2)B[b]	137	6			

[a]Most HCP Ni facets have two possible terminations (labeled as A and B), and the terminations with lower surface energy were used for Wulff construction and subsequent activity study. The corresponding ratios, S_p (%), occupied in the derived morphology are indicated. [b](10$\bar{1}$2) has two terminations with nearly the same surface energy; termination A was used for the activity study below.

FCC Ni morphology is an octahedron-like shape. It contains six inequivalent facets: (111), (100), (221), (111), (211), and (110), ordered by their relative surface ratio occupied, S_p (Table 1). The (111) surface has the lowest E_s of 121 meV/Å^2. It includes eight equivalent surfaces [(111), ($\bar{1}$11), (11$\bar{1}$), (1$\bar{1}$1), ($\bar{1}\bar{1}$1), ($\bar{1}$1$\bar{1}$), (1$\bar{1}\bar{1}$), and ($\bar{1}\bar{1}\bar{1}$)] and covers the surface area S_p of ca. 60% (Table 1). (100) and (221) facets have higher E_s of 138 and 136 meV/Å^2, with S_p of 18% and 8%,

DOI: 10.1021/acs.jpcc.6b08742
J. Phys. Chem. C 2016, 120, 24895−24903

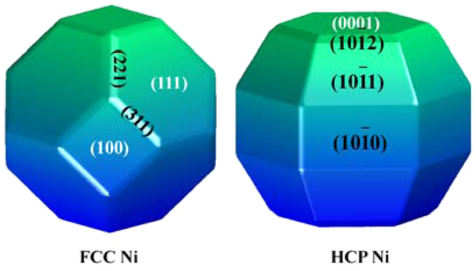

Figure 1. Calculated morphologies of FCC (left) and HCP (right) Ni. The important facets exposed in the morphologies of FCC and HCP Ni are indicated.

respectively. For the exposed facets with even higher surface energies (139−143 meV/Å^2), (311), (211), and (110) cover only a small percentage of surface area, namely, 7%, 4%, and 2%, respectively. It is clear that specific facets exposed as well as the relative ratios exposed are decided by not only their absolute value of surface energies but also their relative orientations.

HCP Ni morphology is very different with a dihedral-like shape. It contains five inequivalent facets, namely, (10$\bar{1}$1), (10$\bar{1}$0) (0001), (10$\bar{1}$2), and (21$\bar{3}$0), ordered by their relative ratio occupied. Although (0001) has the lowest surface energy (E_s = 115 meV/Å^2), it covers only 18% of the total surface area. Actually, the open facets dominate the surface area exposed. For instance, (10$\bar{1}$1) and (10$\bar{1}$0) facets with E_s = 126 and 122 meV/Å^2 cover 48% and 26%, respectively. Finally, (10$\bar{1}$2) and (21$\bar{3}$0) with E_s = 137 and 136 meV/Å^2 cover about 6% and 2% of the total surface area, respectively.

Distinct morphology and facets exposed of FCC and HCP Ni might have great impact on corresponding reactivity, as shown in the CO dissociation below. The derived overall morphologies of FCC and HCP Ni are similar to those of Co,[43] which is understandable because of same crystal symmetries. It is worth noting that the morphologies and facets of FCC and HCP Ni derived here might be influenced by the presence of reactants, alkali additives, particle size, and metal−support interaction.[78,79] However, this is beyond the scope of the present work and the subject of future study.

3.2. Direct CO Dissociation. In this section, we describe direct CO dissociation, where the most stable adsorbed configuration of CO and isolated adsorbed C and O species were used as the initial states for reactant and the final states for product. Key energetics and structural parameters are shown in Table 2. CO adsorption is structure-insensitive, and the calculated adsorption energies, E_{ads}, at their most favorable sites (Table S1 and Figure S1) vary from −1.86 to −1.95 eV only for all FCC and HCP facets considered.

For (111), (0001), and (10$\bar{1}$0), the calculated dissociation barriers, E_a, are as high as 2.96, 2.94, and 2.54 eV, respectively. In line with the huge barriers, their reaction energies, ΔE, are highly endothermic with values of 1.27, 1.23, and 1.18 eV, respectively. For FCC Ni, (311) has the least E_a (1.81 eV) with a modest ΔE of 0.29 eV. The remaining FCC facets, including (110), (100), (221), and (211), have a larger E_a of 1.86, 1.95, 2.00, and 2.01 eV, respectively, and the corresponding calculated ΔE are 0.73, −0.30, 0.55, and 0.20 eV. For HCP Ni,the (10$\bar{1}$2) facet is the most active facet with the least E_a (1.79 eV) and is exothermic ΔE (−0.08 eV), followed by (21$\bar{3}$0) and (10$\bar{1}$1), whose calculated E_a are 1.87 and 1.93 eV with ΔE of 0.72 and 0.02 eV, respectively.

Table 2. Adsorption Energy (E_{ads}) of CO, C, and O at Their Most Favorable Sites; Direct CO Dissociation Barrier (E_a) and Reaction Energy (ΔE) (in eV); and Distance between C and O Atoms at the Transition State (d^{TS}, in Å)

	E_{ads}					
FCC	CO	C	O	E_a	ΔE	d^{TS}
(111)	−1.87	−6.75	−5.38	2.96	1.27	1.83
(100)	−1.90	−8.09	−5.64	1.95	−0.30	1.93
(221)	−1.94	−7.34	−5.59	2.00	0.55	1.95
(311)	−1.90	−7.77	−5.38	1.81	0.29	1.81
(211)	−1.94	−7.75	−5.51	2.01	0.20	2.23
(110)	−1.86	−7.45	−5.21	1.86	0.73	1.96
	E_{ads}					
HCP	CO	C	O	E_a	ΔE	d^{TS}
(10$\bar{1}$1)	−1.95	−7.92	−5.54	1.93	0.02	1.78
(10$\bar{1}$0)	−1.86	−6.90	−5.31	2.54	1.18	1.87
(0001)	−1.90	−6.80	−5.41	2.94	1.23	1.82
(10$\bar{1}$2)	−1.91	−7.92	−5.59	1.79	−0.08	1.93
(21$\bar{3}$0)	−1.90	−7.30	−5.42	1.87	0.72	1.96

It is clear that direct CO dissociation is highly structure sensitive on both FCC and HCP Ni, in line with our previous work on cobalt.[43] The least E_a calculated is 1.81 eV on (311) for FCC Ni and 1.79 eV on (10$\bar{1}$2) for HCP Ni. The close value of the least E_a calculated on FCC and HCP Ni indicates that FCC and HCP Ni would have similar activity for direct CO dissociation if both facets are available and have similar site density on FCC and HCP Ni catalysts. This is particularly true for clean Ni catalysts operating in the low CO coverage regime, where two facets would occupy a similar surface area of 7% and 6% (Table 1). From the calculated least barrier of 1.79 eV, the rate constant for direct CO dissociation at typical Fishcer−Tropsch reaction temperature of 473 K is less than 8.5 × 10^{-7} s^{-1} by assuming a typical prefactor of 1 × 10^{13} s^{-1} based on Arrhenius equation. Whereas on cobalt catalysts, the least barrier for direct CO dissociation is 1.07 eV[43] and the corresponding rate constant is about 39.7 s^{-1}. The activity of Ni catalysts for CO dissociation is rather low compared to that of cobalt catalyst. This is in line with previous experimental findings.[80−82]

The structure sensitivity of direct CO dissociation mainly comes from the structure sensitivity of adsorption of dissociation products (Table 2). Compared to O adsorption at the 3-fold or bridge sites of FCC and HCP facets, its adsorption at 4-fold sites of (100) and (10$\bar{1}$2) are increased by 0.43 eV for (100) and 0.28 eV for (10$\bar{1}$2). The extent of the structure sensitivity for C adsorption is even stronger. Compared to C adsorption at 3-fold sites on Ni in general, its adsorption energy at the 4-fold sites of (100), (10$\bar{1}$1), and (10$\bar{1}$2) facets increases by 1.34 and 1.12 eV at most for FCC Ni and HCP Ni, respectively.

To see more clearly how CO dissociates on FCC and HCP Ni, the transition states (TSs) are plotted in Figures 2 and 3, respectively. From the optimized TSs, the facets with a relative low E_a (1.79−2.01 eV) could be rationalized as follows: (1) For (10$\bar{1}$2), (311), (10$\bar{1}$1), and (100) facets with barriers of 1.79, 1.81, 1.93, and 1.95 eV, respectively, the stronger binding of C atom at the favorable 4-fold sites is the main driving force stabilizing the TSs. (2) For (211) surface with barrier of 2.01 eV, there no surface Ni atoms are shared by C and O. Accordingly, there is no site competition or repulsion, which is

DOI: 10.1021/acs.jpcc.6b08742
J. Phys. Chem. C 2016, 120, 24895−24903

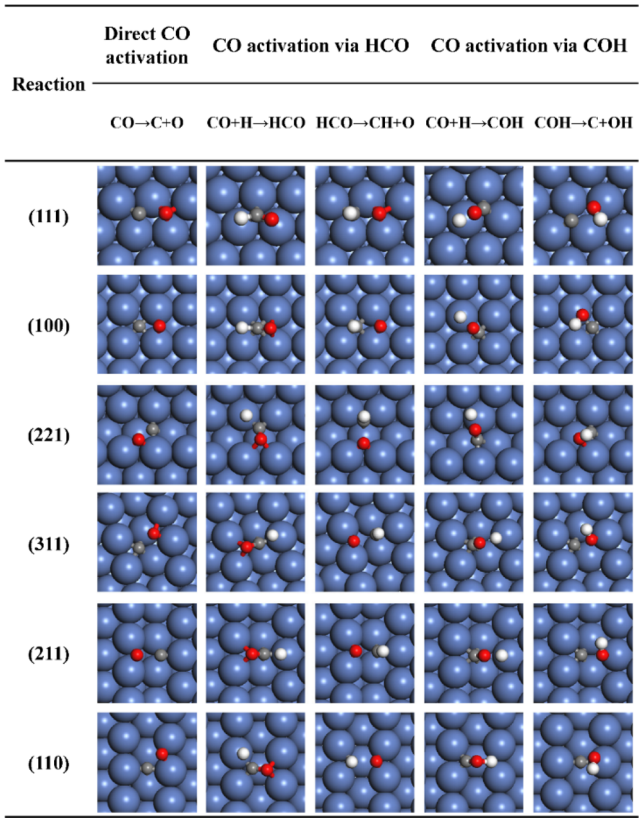

Figure 2. Top view of the transition states of direct CO dissociation and H-assisted CO activation via HCO and HCO intermediates on FCC Ni. Blue, red, gray, and white balls represent Ni, O, C, and H atoms, respectively. This notation is used throughout this paper without mention otherwise.

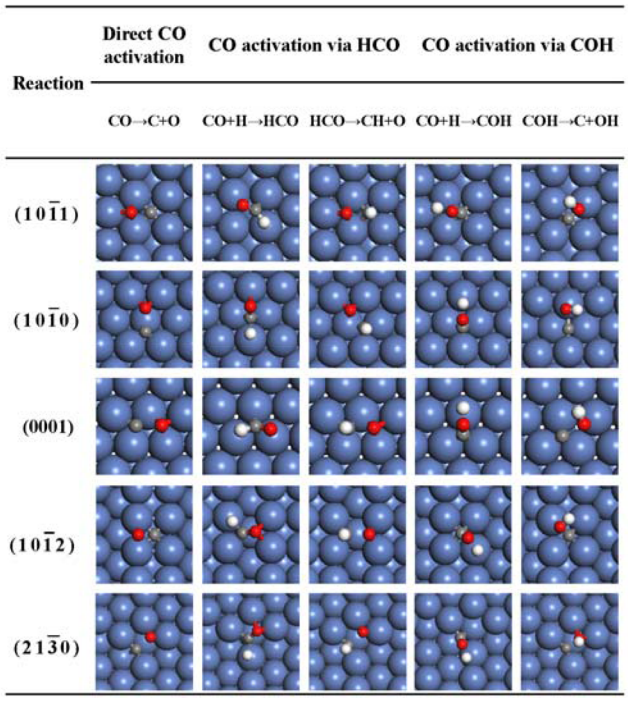

Figure 3. Top view of the transition states of direct CO dissociation and H-assisted CO activation via HCO and HCO intermediates on HCP Ni.

favorable for a lower barrier. (3) For (110), (21$\bar{3}$0), and (221) facets with barrier of 1.86, 1.87, and 2.00 eV, C adsorbs at the long bridge 4-fold like sites, sharing zero or only one surface Ni atoms with O. In contrast, for (10$\bar{1}$0), (0001), and (111) facets with much larger barrier of 2.54, 2.94, and 2.96 eV, respectively, C and O bind exclusively at the 3-fold sites, and both C and O share at least one surface Ni atoms. It is clear that the presence of four-fold sites and the absence or weak site competition for C and O at the TSs are the key for direct CO dissociation with a relative low barrier on Ni catalysts. We note that the bond distance between C and O at the all optimized TSs are larger than 1.78 Å, indicating clearly that direct CO dissociation on Ni passes through a late-transition state.

3.3. H-Assisted CO Dissociation via HCO. In the presence of hydrogen, CO dissociation can proceed via HCO or COH intermediate.[43,67,83−85] In this section, we report the pathway via HCO, namely, CO + H → HCO → CH + O. First, the calculated dissociative adsorption energies of atomic H with respect to $1/2H_2$ in the gas phase fall in the range of −0.46 to −0.57 eV among all the FCC and HCP Ni facets considered. This implies that the structure sensitivity for H adsorption is weak. However, the adsorption of HCO and CH intermediates is structure-sensitive. As seen from Figures S1 and S2, HCO binds the surfaces through both C and O atoms while CH through C atom only. The calculated adsorption energies vary in magnitude by 0.63 eV on all the FCC and HCP Ni facets exposed (Table S2).

The key energetics and structural data for the CO activation via HCO are shown in Table 3. The initial and final states of the elementary reaction steps are taken to be the most stable states of the species in separate adsorption. Because CO and H adsorption are less structure-sensitive, the energetics for CO + H → HCO are largely determined by adsorption of HCO. From Table 3, it can be found that irrespective of the Ni facets and crystal phases considered, corresponding reaction energies, ΔE_1, are highly endothermic. Specifically, calculated ΔE_1 values vary from 0.69 to 1.27 eV on FCC Ni and from 0.94 to 1.27 eV on HCP Ni. The calculated barriers, E_{a1}, fall in the range of 0.93−1.40 eV on FCC Ni and 1.03−1.46 eV on HCP Ni. By careful examination of the TSs, we find that HCO formation mainly involves CO bending and H diffusion.

For HCO → CH + O, calculated reaction energetics, ΔE_2, is exclusively exothermic, irrespective to the crystal phases and facets considered. Specifically, the calculated ΔE_2 vary from −0.78 to −0.08 eV on FCC Ni and from −0.88 to −0.49 eV on HCP Ni. The corresponding calculated barriers, E_{a2}, fall in range of 0.86−1.30 eV for FCC Ni and 0.77−1.06 eV for HCP Ni, respectively. Compared to direct C−O bond breaking of CO, C−O bond breaking for HCO is not demanding and less structure-sensitive. Because both C and O of adsorbed HCO coordinate with surface Ni atoms, C−O bond of adsorbed HCO is already preactivated. This facilitates greatly the subsequent bond breaking, as pointed out in our previous work.[86]

The overall barriers, E_a, and reaction energies, ΔE, for H-assisted CO dissociation (CO + H → CH + O) are listed in Table 3. It can be found that the overall barriers vary from 1.80 to 2.30 eV, and the magnitude of barrier variation is 0.50 eV. Compared to CO direct dissociation with E_a varying from 1.79 to 2.96 eV and barrier variation in magnitude of 1.17 eV, the extent of structure sensitivity of CO dissociation via CHO is weakened significantly. The most active facets are (110) and (21$\bar{3}$0) with E_a of 1.80 eV, followed by (10$\bar{1}$2), (211), and

DOI: 10.1021/acs.jpcc.6b08742
J. Phys. Chem. C 2016, 120, 24895−24903

Table 3. Calculated Key Energies and Structures for H-Assisted CO Dissociation via HCO Intermediate on Each Facet of FCC and HCP Ni[a]

	CO + H → HCO			HCO → CH + O			CO + H → CH + O	
surface	E_{a1}	ΔE_1	d_1	E_{a2}	ΔE_2	d_2	E_a	ΔE
				FCC Ni				
(111)	1.40	1.22	1.16	1.08	−0.43	1.79	2.30	0.79
(100)	1.27	0.69	1.27	1.30	−0.78	1.87	1.99	−0.09
(221)	1.36	1.27	1.49	0.89	−0.67	1.93	2.17	0.60
(311)	1.11	0.96	1.60	0.88	−0.42	1.97	1.85	0.54
(211)	1.10	0.98	1.55	0.86	−0.55	1.96	1.84	0.43
(110)	0.93	0.83	1.54	0.96	−0.08	1.99	1.80	0.75
				HCP Ni				
$(10\bar{1}1)$	1.46	1.06	1.25	0.97	−0.80	1.75	2.03	0.26
$(10\bar{1}0)$	1.31	1.27	1.47	0.79	−0.49	1.77	2.06	0.78
(0001)	1.42	1.22	1.16	1.06	−0.49	1.79	2.29	0.73
$(10\bar{1}2)$	1.03	0.94	1.55	0.89	−0.88	1.93	1.83	0.06
$(21\bar{3}0)$	1.40	1.04	1.65	0.77	−0.52	1.94	1.80	0.52

[a] E_{a1} (E_2) and ΔE_{a1} (ΔE_2) are assigned to elementary reaction barriers and reaction energies, respectively. d_1 (d_2) (in angstroms) is the distance between the C and H atom (or O atom) at the transition states. E_a and ΔE are the overall activation energy and reaction energy for the CO + H → CH + O process, respectively. Energy unit is electronvolt.

Table 4. Calculated Key Energies and Structures for H-Assisted CO Dissociation via COH Intermediate on FCC and HCP Ni[a]

	CO + H → COH			COH → C + OH			CO + H → C + OH	
surface	E_{a1}	ΔE_1	d_1	E_{a2}	ΔE_2	d_2	E_a	ΔE
				FCC Ni				
(111)	1.89	0.95	1.34	1.95	0.60	2.01	2.91	1.55
(100)	1.67	0.62	1.41	1.01	−0.62	1.99	1.67	0.00
(221)	1.86	1.36	1.31	0.80	−0.71	1.82	2.16	0.65
(311)	1.58	0.97	1.40	0.57	−0.91	2.00	1.58	0.06
(211)	1.52	0.99	1.41	0.75	−0.92	2.08	1.75	0.07
(110)	1.42	1.12	1.25	0.69	−0.75	2.03	1.81	0.37
				HCP Ni				
$(10\bar{1}1)$	1.77	0.84	1.35	1.02	−0.56	1.98	1.86	0.28
$(10\bar{1}0)$	1.70	1.08	1.35	1.39	0.08	2.21	2.47	1.16
(0001)	1.88	0.93	1.34	1.98	0.59	2.01	2.92	1.52
$(10\bar{1}2)$	1.73	0.70	1.40	0.95	−0.85	1.94	1.73	−0.15
$(21\bar{3}0)$	1.69	1.19	1.31	0.79	−0.59	1.78	1.98	0.60

[a] E_{a1} (E_{a2}) and ΔE_1 (ΔE_2) are elementary reaction barriers and reaction energies for COH formation (COH decomposition), respectively. d_1 (d_2) (in angstroms) is the distance between the C and H atom (or O atom) at the transition states. E_a and ΔE are the overall activation energy and reaction energy for CO + H → C + OH, respectively. Energy unit is electronvolt.

(311) with E_a of 1.83, 1.84, and 1.85 eV, respectively. Except (211), these facets remain the most active four facets, as also found in the direct pathway with nearly similar barriers (1.79−1.85 eV). For close-packed (0001) and (111) facets, the calculated barriers for CO dissociation via HCO are 2.29 and 2.30 eV, respectively, which are 0.65 and 0.66 eV lower than those of the direct pathway on the same facets.

3.4. H-Assisted CO Dissociation via COH. CO dissociation through COH intermediate (CO + H → COH → C + OH) on FCC and HCP Ni is described here, and the key data are presented in Table 4. Again, because CO and H adsorptions are less structure-sensitive, the reaction energies for COH formation and subsequent C−O bond breaking would be determined by adsorption of COH, OH, and C. The calculated binding energies of COH and OH intermediates at their most favorable sites (Figures S1 and S2) are listed in Table S2. Typically, COH binds through its C atom at the 3- or 4-fold sites, and calculated binding energies vary from −4.08 to −4.72 eV for FCC Ni and from −4.14 to −4.61 eV for HCP Ni, respectively. OH binds through its O atom at the bridge, 3-fold, or 4-fold sites, and calculated binding energies vary from −3.19 to −3.73 eV on FCC Ni and from −3.20 to −3.69 eV on HCP Ni.

Similar to CHO formation, CO hydrogenation to COH is highly endothermic on all the facets exposed. The calculated formation energy, ΔE_1, varies from 0.62 to 1.36 eV on FCC Ni and from 0.70 to 1.19 eV on HCP Ni, respectively. The facets with the largest barriers, E_{a1}, calculated for COH formation are (111), (221), and (0001) facets with values of 1.89, 1.86, and 1.88 eV, respectively. The facet with the least E_{a1} is (110) with value of 1.42 eV. For the remaining facets, the calculated E_{a1} values vary from 1.52 to 1.67 eV for FCC Ni and from 1.69 to 1.77 eV for HCP Ni. Compared to CHO formation, the barriers for COH formation are higher because of the different TSs (Figures 2 and 3): the C−O bond has to be stretched longer (ca. 1.3−1.4 Å) and be crooked for O−H bond formation, costing more energy.

Subsequent C−O bond scission of formed COH is facile. It is exothermic with ΔE_2 from −0.56 to −0.92 eV on most of the facets considered, except $(10\bar{1}0)$, (0001), and (111) with

DOI: 10.1021/acs.jpcc.6b08742
J. Phys. Chem. C 2016, 120, 24895−24903

endothermic ΔE_2 of 0.08, 0.59, and 0.60 eV, respectively. In line with the endothermic reaction energetics for the last three facets, their C−O bond scission barriers are demanding with values of 1.39, 1.98, and 1.95 eV, respectively. Whereas for all remained facets with exothermic ΔE_2, the calculated barriers, E_{a2}, are less than 1 eV. The favorable reaction energetics and lower barriers could be rationalized by the presence of 4-fold sites accommodating a C atom (Figures 2 and 3).

The overall reaction barriers and energies, E_a and ΔE, respectively, for CO dissociation via COH intermediate (CO + H → C + OH) are presented in Table 4. Among all the facets considered, (311) is the most active one with the least E_a of 1.58 eV, followed by (100) and (10$\bar{1}$2) with E_a of 1.67 and 1.73 eV, respectively. These barriers are even lower than the least barriers of direct dissociation and dissociation via CHO calculated so far. This indicates that CO dissociation via COH on these facets are the most favorable and active pathway for CO dissociation. For the remaining facets, calculated E_a values vary in the range of 1.75−2.92 eV. The overall variation of E_a in magnitude of 1.34 eV for all facets considered implies that CO dissociation via COH is structural highly sensitive. The origin could be attributed to the pronounced structure sensitivity of C atom adsorption dissociated from COH.

3.5. FCC Ni versus HCP Ni. Figure 4 shows the (overall) barrier for CO direct dissociation and H-assisted dissociation via HCO and COH on FCC and HCP Ni. Except (221) with barrier of 1.95 eV, H-assisted CO dissociation has relative lower barriers, indicating it is kinetically more favorable than direct dissociation. For (311), (100), (10$\bar{1}$2), (211), and (10$\bar{1}$1) facets, CO dissociation via CO + H → COH → C + OH is preferential, and the corresponding barrier increases gradually from 1.58 to 1.86 eV. A common feature for these low-barrier pathways is the presence of the favorable 4-fold sites accommodating the dissociated C atom. For the remaining Ni facets (110), (21$\bar{3}$0), (10$\bar{1}$0), and (111), CO dissociation via CO + H → HCO → CH + O is favorable, and the corresponding overall barriers are 1.80, 1.80, 2.06, and 2.30 eV, respectively.

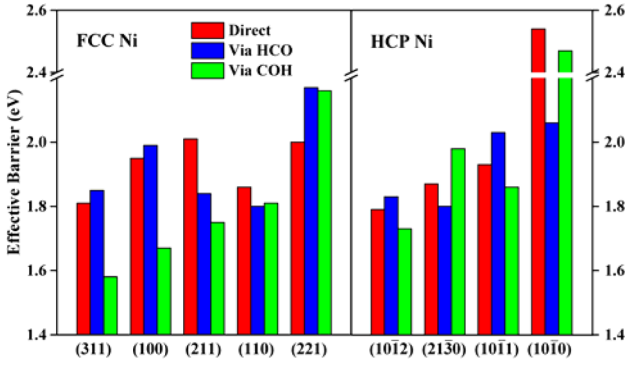

Figure 4. Calculated overall barriers for CO direct dissociation CO → C + O (red) and H-assisted dissociation via CO + H → HCO → CH + O (blue) and CO + H → COH → C + OH (green) on FCC Ni (left) and HCP Ni (right).

These results indicate that (311), (100), (10$\bar{1}$2), (211), and (10$\bar{1}$1) facets not only are more active than the remained Ni facets but also prefer a different dissociation pathway, namely, via COH intermediate rather than CHO intermediates. From Figure 4, it can be found further that the magnitude of barrier variation for CO dissociation via COH intermediate, direct pathway, and CHO intermediate on different Ni facets and crystal phases are 1.34, 1.17, and 0.50 eV, respectively. The larger structural sensitivity for the former two pathways might originate from the larger structural sensitivity of their common product C atom again.

We now turn to comparing the activity of CO dissociation on FCC Ni and HCP Ni. For FCC Ni, our calculations show that the most active facet is (311) with an overall barrier of 1.58 eV, while the next active facet is (100) with an overall barrier of 1.67 eV. For HCP Ni, the most active facet is (10$\bar{1}$2) witha barrier of 1.73 eV. This result tells that for CO dissociation on Ni, FCC Ni would have a higher intrinsic activity than HCP Ni. Moreover, based on the optimized FCC and HCP morphology, (311) and (100) occupy 7% and 18% of FCC Ni surface, respectively, whereas 6% for HCP (10$\bar{1}$2). This implies that the corresponding site density of FCC Ni is about four times larger than that of HCP Ni. In brief, FCC Ni would be more active than HCP Ni because of the higher intrinsic activity and denser active sites.

3.6. Ni versus Co. We studied CO dissociation on HCP and FCC Co in the past[43] and compare their difference with Ni below. This comparison is meaningful because nearly the same computational parameters were used in both works. First, the intrinsic activity of Ni for CO dissociation is lower than that for Co. For Ni, the least barrier for CO dissociation is 1.56 eV on FCC (311). For Co, there are at least seven facets including (10$\bar{1}$1), (11$\bar{2}$1), (10$\bar{1}$2), (11$\bar{2}$0), (311), (110,) and (100) whose barriers are lower than the most active FCC Ni(311). Second, the preferential pathway for CO dissociation is different. For Ni, as found above, H-assisted CO dissociation is the dominate pathway on both FCC and HCP phases. Whereas for Co, CO direct dissociation is preferential on the HCP phase, and H-assisted CO dissociation is preferential on the FCC phase. Finally, dependence of activity on the crystal phases is also different. For Ni, the FCC phase not only has higher intrinsic activity (lower CO dissociation barrier) but also has denser active sites than that of HCP phases. This is exactly the opposite to Co. That is, HCP Co has not only higher intrinsic activity but also denser active sites than FCC Co.

We take the FCC (100) surface as an example to rationalize the difference between Ni and Co on CO dissociation. On Ni and Co (100) surfaces, the energetics for the reactants (CO and H) and the products (C, O, CH, and OH) involved in CO dissociation are tabulated in Figure 5 and Table S3. Preferential adsorption sites for CO, H, C, O, CH, and OH (4-fold site) as

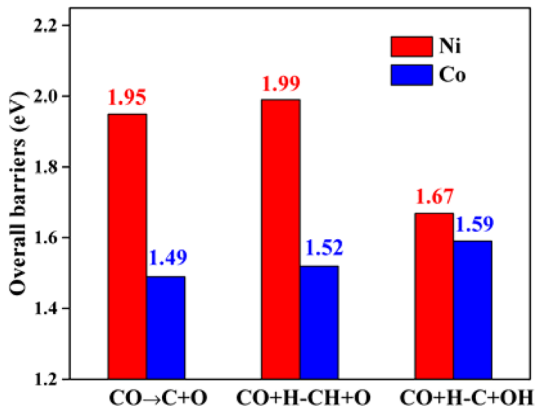

Figure 5. Overall reaction barriers for CO activation through three pathways over FCC (100) surface of Co and Ni.

DOI: 10.1021/acs.jpcc.6b08742
J. Phys. Chem. C 2016, 120, 24895−24903

well as the optimized transition states (Figures 2 and 3) are almost the same on both Ni(100) and Co(100), a fact that facilitates the comparison.

On Ni(100), the binding strengths of the reactant CO and H are about 0.19 and 0.10 eV stronger than those on Co(100). However, the product O and OH on Ni(100) are 0.35 and 0.19 eV weaker than those on Co(100), but for the product C and CH stronger by 0.08 and 0.14 eV, respectively. These lead to CO dissociation on Ni being energetically less favorable than Co. As seen from Table S3, the calculated overall reaction energies, ΔE, on Ni(100) are less exothermic than that on Co(100) by at least 0.37 eV, irrespective of CO direct dissociation or H-assisted dissociation via COH and CHO. Because their transition states are similar, the less exothermic reaction energetics on Ni(100) results in a higher dissociation barrier, E_a, as shown in Figure 5 and Table S3. Accordingly, Ni is less active than Co to dissociate CO. Actually, CO direct dissociation on Ni(100) is so demanding, with a barrier of 1.95 eV, that an alternative pathway in the H-assisted dissociation via COH becomes kinetically preferred with a lower barrier of 1.67 eV. Co(100) is more active and can dissociate CO directly with a modest barrier of 1.49 eV. This actually leaves a little room for H-assisted dissociation via CHO or COH to compete direct dissociation.

4. CONCLUSION

A systemic DFT study of crystal phase dependence of CO dissociation on Ni is presented. On the basis of calculated surface energies and Wulff construction, we first optimize the morphologies for FCC and HCP Ni. The facets exposed are used to investigate CO dissociation and the influence of crystal phases. On both FCC and HCP Ni phases, CO dissociation presents a large structural sensitivity. Irrespective of the crystal phases, CO dissociation assisted by hydrogen is kinetically more favorable than that of direct dissociation. CO dissociation prefers the COH intermediate but changes to the CHO intermediate with increase of the barrier. The most active facet is (311), followed by (100), (10$\bar{1}$2), (211), and (10$\bar{1}$1). Compared to HCP Ni, FCC Ni exposes more facets with lower barriers. The distinct behaviors of different crystal phases (FCC versus HCP) and dependence on composition (Ni versus Co) revealed here are valuable for optimization of catalysts to expose abundant active sites activating diatomic molecules. Further study of the influence of the crystal phases on methanation and C−C coupling will be carried out in future contributions.

■ ASSOCIATED CONTENT

Supporting Information

The Supporting Information is available free of charge on the ACS Publications website at DOI: 10.1021/acs.jpcc.6b08742.

Calculated binding energies and the favorable adsorption configurations of the intermediates involved in direct CO activation (Table S1) and in H-assisted CO activation (Table S2); energetic information for CO activation over FCC (100) surface of Co and Ni (Table S3); and structural information for adsorption of CO, C, O, H, HCO, CH, COH, and OH intermediates on FCC Ni (Figure S1) and HCP Ni (Figure S2) (PDF)

■ AUTHOR INFORMATION

Corresponding Author

*Tel.: +86-551-6360 0650. E-mail: wxli70@ustc.edu.cn.

Notes

The authors declare no competing financial interest.

■ ACKNOWLEDGMENTS

We are grateful for the finanical support from the Natural Science Foundation of China (21273224, 21321002, 21225315) and the National Basic Research Program of China (2013CB834603).

■ REFERENCES

(1) Karelovic, A.; Ruiz, P. Mechanistic Study of Low Temperature CO2Methanation over Rh/TiO2 Catalysts. *J. Catal.* **2013**, *301*, 141−153.

(2) Wang, Z.-j.; Skiles, S.; Yang, F.; Yan, Z.; Goodman, D. W. Particle Size Effects in Fischer−Tropsch Synthesis by Cobalt. *Catal. Today* **2012**, *181*, 75−81.

(3) Carballo, J. M. G.; Yang, J.; Holmen, A.; García-Rodríguez, S.; Rojas, S.; Ojeda, M.; Fierro, J. L. G. Catalytic Effects of Ruthenium Particle Size on the Fischer−Tropsch Synthesis. *J. Catal.* **2011**, *284*, 102−108.

(4) Prieto, G.; Martínez, A.; Concepción, P.; Moreno-Tost, R. Cobalt Particle Size Effects in Fischer−Tropsch Synthesis: Structural and in situ Spectroscopic Characterisation on Reverse Micelle-Synthesised Co/Itq-2 Model Catalysts. *J. Catal.* **2009**, *266*, 129−144.

(5) Herranz, T.; Deng, X.; Cabot, A.; Guo, J.; Salmeron, M. Influence of the Cobalt Particle Size in the Co Hydrogenation Reaction Studied by in Situ X-Ray Absorption Spectroscopy. *J. Phys. Chem. B* **2009**, *113*, 10721−10727.

(6) Den Breejen, J.; Radstake, P.; Bezemer, G.; Bitter, J.; Froseth, V.; Holmen, A.; Jong, K. P. On the Origin of the Cobalt Particle Size Effects in Fischer−Tropsch Catalysis. *J. Am. Chem. Soc.* **2009**, *131*, 7197.

(7) Newton, M. A.; Dent, A. J.; Fiddy, S. G.; Jyoti, B.; Evans, J. Particle Size Effects in Rh/Al2O3 Catalysts as Viewed from a Structural, Functional, and Reactive Perspective: The Case of the Reactive Adsorption of No. *J. Mater. Sci.* **2007**, *42*, 3288−3298.

(8) Bezemer, G. L.; Bitter, J. H.; Kuipers, H. P.; Oosterbeek, H.; Holewijn, J. E.; Xu, X.; Kapteijn, F.; van Dillen, A. J.; de Jong, K. P. Cobalt Particle Size Effects in the Fischer−Tropsch Reaction Studied with Carbon Nanofiber Supported Catalysts. *J. Am. Chem. Soc.* **2006**, *128*, 3956−3964.

(9) Abad, A.; Concepción, P.; Corma, A.; García, H. A Collaborative Effect between Gold and a Support Induces the Selective Oxidation of Alcohols. *Angew. Chem., Int. Ed.* **2005**, *44*, 4066−4069.

(10) Comotti, M.; Li, W.-C.; Spliethoff, B.; Schüth, F. Support Effect in High Activity Gold Catalysts for Co Oxidation. *J. Am. Chem. Soc.* **2006**, *128*, 917−924.

(11) Zhou, K.; Li, Y. Catalysis Based on Nanocrystals with Well-Defined Facets. *Angew. Chem., Int. Ed.* **2012**, *51*, 602−613.

(12) Lee, H.; Habas, S. E.; Kweskin, S.; Butcher, D.; Somorjai, G. A.; Yang, P. Morphological Control of Catalytically Active Platinum Nanocrystals. *Angew. Chem.* **2006**, *118*, 7988−7992.

(13) Mclaren, A.; Valdes-Solis, T.; Li, G.; Tsang, S. C. Shape and Size Effects of Zno Nanocrystals on Photocatalytic Activity. *J. Am. Chem. Soc.* **2009**, *131*, 12540−12541.

(14) Liu, J.-X.; Su, H.-Y.; Li, W.-X. Structure Sensitivity of Co Methanation on Co(0001), (10−12) and (11−20) Surfaces: Density Functional Theory Calculations. *Catal. Today* **2013**, *215*, 36−42.

(15) Green, I. X.; Tang, W.; Neurock, M.; Yates, J. T. Spectroscopic Observation of Dual Catalytic Sites During Oxidation of Co on a Au/Tio2 Catalyst. *Science* **2011**, *333*, 736−739.

(16) Fu, Q.; et al. Interface-Confined Ferrous Centers for Catalytic Oxidation. *Science* **2010**, *328*, 1141−1144.

DOI: 10.1021/acs.jpcc.6b08742
J. Phys. Chem. C 2016, 120, 24895−24903

(17) Graciani, J.; Mudiyanselage, K.; Xu, F.; Baber, A. E.; Evans, J.; Senanayake, S. D.; Stacchiola, D. J.; Liu, P.; Hrbek, J.; Sanz, J. F.; et al. Highly Active Copper-Ceria and Copper-Ceria-Titania Catalysts for Methanol Synthesis from Co2. *Science* **2014**, *345*, 546−550.
(18) Dong, W.; et al. Co−Co_2c and Co−Co_2c/Ac Catalysts for Hydroformylation of 1-Hexene under Low Pressure: Experimental and Theoretical Studies. *J. Phys. Chem. C* **2014**, *118*, 19114−19122.
(19) Pei, Y.-P.; et al. High Alcohols Synthesis Via Fischer−Tropsch Reaction at Cobalt Metal/Carbide Interface. *ACS Catal.* **2015**, *5*, 3620−3624.
(20) Behrens, M.; Studt, F.; Kasatkin, I.; Kühl, S.; Hävecker, M.; Abild-Pedersen, F.; Zander, S.; Girgsdies, F.; Kurr, P.; Kniep, B.-L.; et al. The Active Site of Methanol Synthesis over Cu/ZnO/Al2O3 Industrial Catalysts. *Science* **2012**, *336*, 893−897.
(21) Norskov, J. K.; Bligaard, T.; Rossmeisl, J.; Christensen, C. H. Towards the Computational Design of Solid Catalysts. *Nat. Chem.* **2009**, *1*, 37−46.
(22) Ducreux, O.; Rebours, B.; Lynch, J.; Roy-Auberger, M.; Bazin, D. Microstructure of Supported Cobalt Fischer−Tropsch Catalysts. *Oil Gas Sci. Technol.* **2009**, *64*, 49−62.
(23) Ducreux, O.; Lynch, J.; Rebours, B.; Roy, M.; Chaumette, P. *In-Situ* Characterisation of Cobalt Based Fischer−Tropsch Catalysts: A New Approach to the Active Phase. *Stud. Surf. Sci. Catal.* **1998**, *119*, 125−130.
(24) Khodakov, A. Y. Fischer−Tropsch Synthesis: Relations between Structure of Cobalt Catalysts and Their Catalytic Performance. *Catal. Today* **2009**, *144*, 251−257.
(25) Sadeqzadeh, M.; Karaca, H.; Safonova, O.; Fongarland, P.; Chambrey, S.; Roussel, P.; Griboval-Constant, A.; Lacroix, M.; Curulla-Ferré, D.; Luck, F.; et al. Identification of the Active Species in the Working Alumina-Supported Cobalt Catalyst under Various Conditions of Fischer−Tropsch Synthesis. *Catal. Today* **2011**, *164*, 62−67.
(26) Zhang, Q.; Deng, W.; Wang, Y. Recent Advances in Understanding the Key Catalyst Factors for Fischer−Tropsch Synthesis. *J. Energy Chem.* **2013**, *22*, 27−38.
(27) de la Peña O'Shea, V. A.; de la Piscina, P. R.; Homs, N.; Aromí, G.; Fierro, J. L. G. Development of Hexagonal Closed-Packed Cobalt Nanoparticles Stable at High Temperature. *Chem. Mater.* **2009**, *21*, 5637−5643.
(28) Kusada, K.; Kobayashi, H.; Yamamoto, T.; Matsumura, S.; Sumi, N.; Sato, K.; Nagaoka, K.; Kubota, Y.; Kitagawa, H. Discovery of Face-Centered-Cubic Ruthenium Nanoparticles: Facile Size-Controlled Synthesis Using the Chemical Reduction Method. *J. Am. Chem. Soc.* **2013**, *135*, 5493−5496.
(29) Mou, X.; Zhang, B.; Li, Y.; Yao, L.; Wei, X.; Su, D. S.; Shen, W. Rod-Shaped Fe_2o_3 as an Efficient Catalyst for the Selective Reduction of Nitrogen Oxide by Ammonia. *Angew. Chem., Int. Ed.* **2012**, *51*, 2989−2993.
(30) Liu, J.-X.; Li, W.-X. Theoretical Study of Crystal Phase Effect in Heterogeneous Catalysis. *WIREs: Comput. Mol. Sci.* **2016**, *6*, 571.
(31) Ye, H.; Wang, Q.; Catalano, M.; Lu, N.; Vermeylen, J.; Kim, M. J.; Liu, Y.; Sun, Y.; Xia, X. Ru Nanoframes with an Fcc Structure and Enhanced Catalytic Properties. *Nano Lett.* **2016**, *16*, 2812−2817.
(32) Yao, Y.; He, D. S.; Lin, Y.; Feng, X.; Wang, X.; Yin, P.; Hong, X.; Zhou, G.; Wu, Y.; Li, Y. Modulating Fcc and Hcp Ruthenium on the Surface of Palladium−Copper Alloy through Tunable Lattice Mismatch. *Angew. Chem.* **2016**, *128*, 5591−5595.
(33) Zhao, M.; Figueroa-Cosme, L.; Elnabawy, A.; Vara, M. I.; Yang, X.; Roling, L.; Chi, M.; Mavrikakis, M.; Xia, Y. Synthesis and Characterization of Ru Cubic Nanocages with a Face-Centered-Cubic (Fcc) Structure by Templating with Pd Nanocubes. *Nano Lett.* **2016**, *16*, 5310.
(34) Liu, J. X.; Li, W. X. Theoretical Study of Crystal Phase Effect in Heterogeneous Catalysis. *Wiley Interdisciplinary Reviews: Computational Molecular Science* **2016**, *6*, 571.
(35) Song, C.; Sakata, O.; Kumara, L. S. R.; Kohara, S.; Yang, A.; Kusada, K.; Kobayashi, H.; Kitagawa, H. Size Dependence of Structural Parameters in Fcc and Hcp Ru Nanoparticles, Revealed by Rietveld Refinement Analysis of High-Energy X-Ray Diffraction Data. *Sci. Rep.* **2016**, *6*, 31400.
(36) Kusada, K.; Kitagawa, H. A Route for Phase Control in Metal Nanoparticles: A Potential Strategy to Create Advanced Materials. *Adv. Mater.* **2016**, *28*, 1129−1142.
(37) Gu, J.; Guo, Y.; Jiang, Y.-Y.; Zhu, W.; Xu, Y.-S.; Zhao, Z.-Q.; Liu, J.-X.; Li, W.-X.; Jin, C.-H.; Yan, C.-H.; et al. Robust Phase Control through Hetero-Seeded Epitaxial Growth for Face-Centered Cubic Pt@ Ru Nanotetrahedrons with Superior Hydrogen Electro-Oxidation Activity. *J. Phys. Chem. C* **2015**, *119*, 17697−17706.
(38) Gnanamani, M. K.; Jacobs, G.; Shafer, W. D.; Davis, B. H. Fischer−Tropsch Synthesis: Activity of Metallic Phases of Cobalt Supported on Silica. *Catal. Today* **2013**, *215*, 13−17.
(39) Kitakami, O.; Sato, H.; Shimada, Y.; Sato, F.; Tanaka, M. Size Effect on the Crystal Phase of Cobalt Fine Particles. *Phys. Rev. B: Condens. Matter Mater. Phys.* **1997**, *56*, 13849.
(40) Fischer, N.; van Steen, E.; Claeys, M. Preparation of Supported Nano-Sized Cobalt Oxide and Fcc Cobalt Crystallites. *Catal. Today* **2011**, *171*, 174−179.
(41) Braconnier, L.; Landrivon, E.; Clémençon, I.; Legens, C.; Diehl, F.; Schuurman, Y. How Does Activation Affect the Cobalt Crystallographic Structure? An in Situ Xrd and Magnetic Study. *Catal. Today* **2013**, *215*, 18−23.
(42) Prieto, G.; Concepción, P.; Murciano, R.; Martínez, A. The Impact of Pre-Reduction Thermal History on the Metal Surface Topology and Site-Catalytic Activity of Co/Sio2 Fischer−Tropsch Catalysts. *J. Catal.* **2013**, *302*, 37−48.
(43) Liu, J.-X.; Su, H.-Y.; Sun, D.-P.; Zhang, B.-Y.; Li, W.-X. Crystallographic Dependence of Co Activation on Cobalt Catalysts: Hcp Versus Fcc. *J. Am. Chem. Soc.* **2013**, *135*, 16284−16287.
(44) Coenen, J.; Van Nisselrooy, P.; De Croon, M.; Van Dooren, P.; Van Meerten, R. The Dynamics of Methanation of Carbon Monoxide on Nickel Catalysts. *Appl. Catal.* **1986**, *25*, 1−8.
(45) Kustov, A. L.; Frey, A. M.; Larsen, K. E.; Johannessen, T.; Norskov, J. K.; Christensen, C. H. CO Methanation over Supported Bimetallic Ni-Fe Catalysts: From Computational Studies Towards Catalyst Optimization. *Appl. Catal., A* **2007**, *320*, 98−104.
(46) Ho, S. V.; Harriott, P. The Kinetics of Methanation on Nickel Catalysts. *J. Catal.* **1980**, *64*, 272−283.
(47) Illy, S.; Tillement, O.; Machizaud, F.; Dubois, J.; Massicot, F.; Fort, Y.; Ghanbaja, J. First Direct Evidence of Size-Dependent Structural Transition in Nanosized Nickel Particles. *Philos. Mag. A* **1999**, *79*, 1021−1031.
(48) Hemenger, P.; Weik, H. On the Existence of Hexagonal Nickel. *Acta Crystallogr.* **1965**, *19*, 690−691.
(49) Mi, Y.; Yuan, D.; Liu, Y.; Zhang, J.; Xiao, Y. Synthesis of Hexagonal Close-Packed Nanocrystalline Nickel by a Thermal Reduction Process. *Mater. Chem. Phys.* **2005**, *89*, 359−361.
(50) Han, M.; Liu, Q.; He, J.; Song, Y.; Xu, Z.; Zhu, J. Controllable Synthesis and Magnetic Properties of Cubic and Hexagonal Phase Nickel Nanocrystals. *Adv. Mater.* **2007**, *19*, 1096−1100.
(51) Lahiri, A.; Das, R. Synthesis of Face Centered Cubic and Hexagonal Closed Packed Nickel Using Ionic Liquids. *J. Appl. Electrochem.* **2010**, *40*, 1991−1995.
(52) Lahiri, A.; Das, R.; Reddy, R. G. Electrochemical Synthesis of Hexagonal Closed Pack Nickel: A Hydrogen Storage Material. *J. Power Sources* **2010**, *195*, 1688−1690.
(53) Lahiri, A.; Tadisina, Z. Synthesis, Thermodynamic and Magnetic Properties of Pure Hexagonal Close Packed Nickel. *Mater. Chem. Phys.* **2010**, *124*, 41−43.
(54) Bolokang, A.; Phasha, M. Novel Synthesis of Metastable Hcp Nickel by Water Quenching. *Mater. Lett.* **2011**, *65*, 59−60.
(55) Kotoulas, A.; Gjoka, M.; Simeonidis, K.; Tsiaoussis, I.; Angelakeris, M.; Kalogirou, O.; Dendrinou-Samara, C. The Role of Synthetic Parameters in the Magnetic Behavior of Relative Large Hcp Ni Nanoparticles. *J. Nanopart. Res.* **2011**, *13*, 1897−1908.
(56) Guo, Y.; Azmat, M. U.; Liu, X.; Ren, J.; Wang, Y.; Lu, G. Controllable Synthesis of Hexagonal Close-Packed Nickel Nano-

DOI: 10.1021/acs.jpcc.6b08742
J. Phys. Chem. C 2016, 120, 24895−24903

particles under High Nickel Concentration and Its Catalytic Properties. *J. Mater. Sci.* **2011**, *46*, 4606−4613.
(57) Mavrikakis, M.; Baumer, M.; Freund, H. J.; Norskov, J. K. Structure Sensitivity of Co Dissociation on Rh Surfaces. *Catal. Lett.* **2002**, *81*, 153−156.
(58) Gong, X. Q.; Raval, R.; Hu, P. CO Dissociation and O Removal on Co(0001): A Density Functional Theory Study. *Surf. Sci.* **2004**, *562*, 247−256.
(59) Riedmüller, B.; Ciobîcă, I. M.; Papageorgopoulos, D. C.; Frechard, F.; Berenbak, B.; Kleyn, A. W.; van Santen, R. A. Co Adsorption on Hydrogen Saturated Ru(0001). *J. Chem. Phys.* **2001**, *115*, 5244.
(60) Shetty, S.; van Santen, R. A. CO Dissociation on Ru and Co Surfaces: The Initial Step in the Fischer−Tropsch Synthesis. *Catal. Today* **2011**, *171*, 168−173.
(61) Wang, H.; et al. Platinum-Modulated Cobalt Nanocatalysts for Low-Temperature Aqueous-Phase Fischer−Tropsch Synthesis. *J. Am. Chem. Soc.* **2013**, *135*, 4149−4158.
(62) Zubkov, T.; Morgan, G. A., Jr; Yates, J. T., Jr Spectroscopic Detection of CO Dissociation on Defect Sites on Ru (109): Implications for Fischer−Tropsch Catalytic Chemistry. *Chem. Phys. Lett.* **2002**, *362*, 181−184.
(63) Zubkov, T.; Morgan, G., Jr; Yates, J., Jr; Kühlert, O.; Lisowski, M.; Schillinger, R.; Fick, D.; Jänsch, H. The Effect of Atomic Steps on Adsorption and Desorption of Co on Ru (109). *Surf. Sci.* **2003**, *526*, 57−71.
(64) Pfnür, H.; Feulner, P.; Menzel, D. The Influence of Adsorbate Interactions on Kinetics and Equilibrium for Co on Ru (001). Ii. Desorption Kinetics and Equilibrium. *J. Chem. Phys.* **1983**, *79*, 4613−4623.
(65) Bengaard, H.; Nørskov, J. K.; Sehested, J.; Clausen, B. S.; Nielsen, L. P.; Molenbroek, A. M.; Rostrup-Nielsen, J. R. Steam Reforming and Graphite Formation on Ni Catalysts. *J. Catal.* **2002**, *209*, 365−384.
(66) Engbæk, J.; Lytken, O.; Nielsen, J. H.; Chorkendorff, I. Co Dissociation on Ni: The Effect of Steps and of Nickel Carbonyl. *Surf. Sci.* **2008**, *602*, 733−743.
(67) Andersson, M. P.; Abild-Pedersen, F.; Remediakis, I. N.; Bligaard, T.; Jones, G.; Engbæk, J.; Lytken, O.; Horch, S.; Nielsen, J. H.; Sehested, J. Structure Sensitivity of the Methanation Reaction: H2-Induced CO Dissociation on Nickel Surfaces. *J. Catal.* **2008**, *255*, 6−19.
(68) Kresse, G.; Hafner, J. Ab Initio Molecular Dynamics for Liquid Metals. *Phys. Rev. B: Condens. Matter Mater. Phys.* **1993**, *47*, 558.
(69) Kresse, G.; Furthmüller, J. Efficient Iterative Schemes for Ab Initio Total-Energy Calculations Using a Plane-Wave Basis Set. *Phys. Rev. B: Condens. Matter Mater. Phys.* **1996**, *54*, 11169.
(70) Blöchl, P. E. Projector Augmented-Wave Method. *Phys. Rev. B: Condens. Matter Mater. Phys.* **1994**, *50*, 17953.
(71) Perdew, J. P.; Burke, K.; Ernzerhof, M. Generalized Gradient Approximation Made Simple. *Phys. Rev. Lett.* **1996**, *77*, 3865−3868.
(72) Monkhorst, H. J.; Pack, J. D. Special Points for Brillouin-Zone Integrations. *Phys. Rev. B* **1976**, *13*, 5188−5192.
(73) Taylor, A. Lattice Parameters of Binary Nickel Cobalt Alloys. *J. Inst. Metals* **1950**, *77*, 585−594.
(74) Wright, J.; Goddard, J. The Lattice Constants and Magnetic Anisotropy Constants of Electrodeposited Single Crystal Films of Hexagonal Close-Packed Nickel. *Philos. Mag.* **1965**, *11*, 485−493.
(75) Sun, K.; Zhao, Y.; Su, H. Y.; Li, W. X. Force Reversed Method for Locating Transition States. *Theor. Chem. Acc.* **2012**, *131*, 1−10.
(76) Henkelman, G.; Uberuaga, B. P.; Jónsson, H. A Climbing Image Nudged Elastic Band Method for Finding Saddle Points and Minimum Energy Paths. *J. Chem. Phys.* **2000**, *113*, 9901.
(77) Henkelman, G.; Jónsson, H. Improved Tangent Estimate in the Nudged Elastic Band Method for Finding Minimum Energy Paths and Saddle Points. *J. Chem. Phys.* **2000**, *113*, 9978.
(78) Huo, C.-F.; Wu, B.-S.; Gao, P.; Yang, Y.; Li, Y.-W.; Jiao, H. The Mechanism of Potassium Promoter: Enhancing the Stability of Active Surfaces. *Angew. Chem., Int. Ed.* **2011**, *50*, 7403−7406.
(79) Hansen, P. L.; Wagner, J. B.; Helveg, S.; Rostrup-Nielsen, J. R.; Clausen, B. S.; Topsøe, H. Atom-Resolved Imaging of Dynamic Shape Changes in Supported Copper Nanocrystals. *Science* **2002**, *295*, 2053−2055.
(80) Ng, L.; Uram, K. J.; Xu, Z.; Jones, P. L.; Yates, J. T. Mechanism of CO Bond Scission at Alkali Promoter Sites—Iras Study of the System Co/K/Ni(111). *J. Chem. Phys.* **1987**, *86*, 6523−6530.
(81) Benndorf, C.; Meyer, L. CO Adsorption on Ni(551). *Surf. Sci.* **1991**, *251*−*252*, 872−876.
(82) Goodwan, D. W.; Kelley, R. D.; Madey, T. E.; White, J. M. Measurement of Carbide Buildup and Removal Kinetics on Ni(100). *J. Catal.* **1980**, *64*, 479−481.
(83) Zhuo, M.; Tan, K. F.; Borgna, A.; Saeys, M. Density Functional Theory Study of the Co Insertion Mechanism for Fischer−Tropsch Synthesis over Co Catalysts. *J. Phys. Chem. C* **2009**, *113*, 8357−8365.
(84) Huo, C.-F.; Li, Y.-W.; Wang, J.; Jiao, H. Formation of Chx Species from Co Dissociation on Double-Stepped Co(0001): Exploring Fischer−Tropsch Mechanism. *J. Phys. Chem. C* **2008**, *112*, 14108−14116.
(85) Ojeda, M.; Nabar, R.; Nilekar, A. U.; Ishikawa, A.; Mavrikakis, M.; Iglesia, E. Co Activation Pathways and the Mechanism of Fischer−Tropsch Synthesis. *J. Catal.* **2010**, *272*, 287−297.
(86) Zhao, Y.-H.; Liu, J.-X.; Su, H.-Y.; Sun, K.; Li, W.-X. A First-Principles Study of Carbon−Oxygen Bond Scission in Multiatomic Molecules on Flat and Stepped Metal Surfaces. *ChemCatChem* **2014**, *6*, 1755−1762.

DOI: 10.1021/acs.jpcc.6b08742
J. Phys. Chem. C 2016, 120, 24895−24903